

CAAP Quarterly Report

Date of Report: 04/18/2020

Prepared for: *U.S. DOT Pipeline and Hazardous Materials Safety Administration*

Contract Number: 693JK31950004CAAP

Project Title: Multi-modal NDE Assisted Probabilistic Pipeline Performance Evaluation under Interactive Anomalies

Prepared by: *Kiswendsida Jules Kere, Karthik Gopalakrishnan, Dr. Vivek Rathod, Qindan Huang, Qixin Zhou, and Yiming Deng*

Contact Information: Qindan Huang, qhuang@uakron.edu, 330-972-6972
Yiming Deng, dengyimi@egr.msu.edu, 517-884-0926
Qixin Zhou, qzhou@uakron.edu, 330-972-7159

For quarterly period ending: 03/29/2020

Business and Activity Section

(a) Contract Activity

No contract modification was made or proposed in this quarterly period. No materials were purchased during this quarterly period.

(b) Status Update of Past Quarter Activities

In the past quarter, we continued making progress in Task 1, Task 2, and Task 3. In particular, we conducted environmental testing on specimens, and characterized the corrosion defect profile with optical microscopy measurement in Task 1. In Task 2, we investigated the detection capability on defects along circumferential direction, and also used an automated signal classification to determine defect characteristics (such as defect depth, length, and location). In Task 3, we modified and updated the database we collected, fine-tuned the ABAQUS model to generate additional cases with a single defect, and re-evaluated the performance of the existing prediction models.

(c) Cost share activity

Partial support for one graduate student tuition and 0.57 months of Dr. Huang's annual year salary was provided by The University of Akron as per the cost share agreement.

(d) Task 1. Generate realistic corrosion and cracking defect profiles

1. Objective of Task 1

The objective of Task 1 is to utilize the experimental testing and numerical analysis to generate more realistic defect shapes and colony profiles, which will be used for characterization and validation of interactive defects using non-destructive evaluation (NDE). Meanwhile, the identified defect profile will be used for the probabilistic defect time-evolution model development, which is crucial for reliability evaluation of pipeline performance under interactive defects.

2. Research Progress in the 2nd Quarter

UAkron and MSU had discussed and finalized the experimental procedures for corrosion exposure testing that involves the corrosion evaluation at UAkron and NDE study at MSU. The metal types and sample sizes were determined in this quarter through consulting with GTI. The metal for the exposure test is a ground low-carbon steel with a similar composition as the API series pipeline metals. The sample is flat sheet with the size of $3'' \times 3'' \times 3/32''$. The samples were in the exposure of 5 wt.% NaCl fog in an environmental chamber following ASTM B117 salt spray testing. One graduate student at UAkron was working this task.

The optical microscopy measurement was conducted on the metal surface. The preliminary testing result from optical microscopy is shown in Figure 1. In addition, the time evolution of corrosion profile was characterized by infinite focus microscopy as shown in Figure 2. It is expected to obtain the length, width, and depth of the corrosion defects. The exposure testing was conducting around 2 weeks. Due to the pandemic of COVID-19, UAkron has switched to on-line classes and non-essential research has stopped. Therefore, the exposure testing had to be stopped for now.

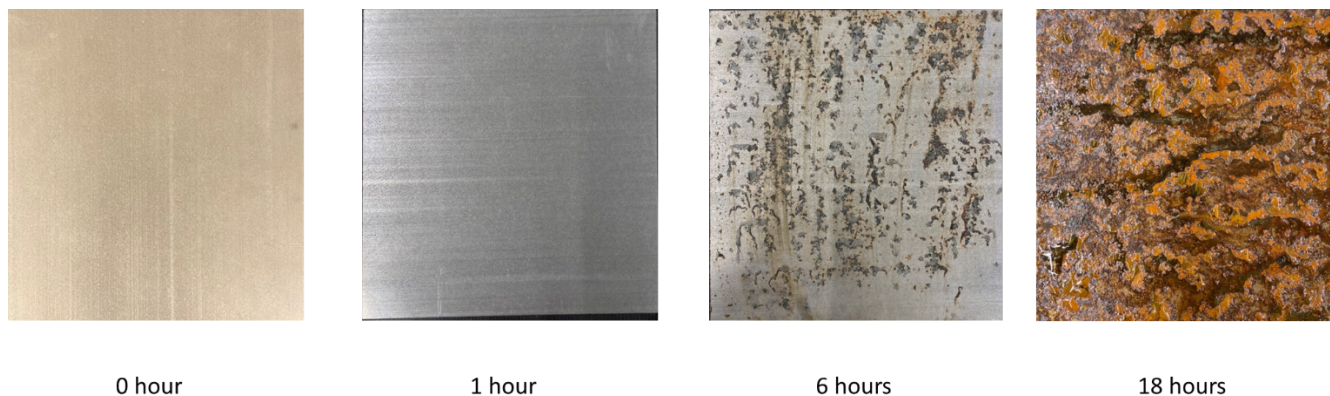


Figure 1. Optical microscopy observations on the metal surface under salt fog exposure.

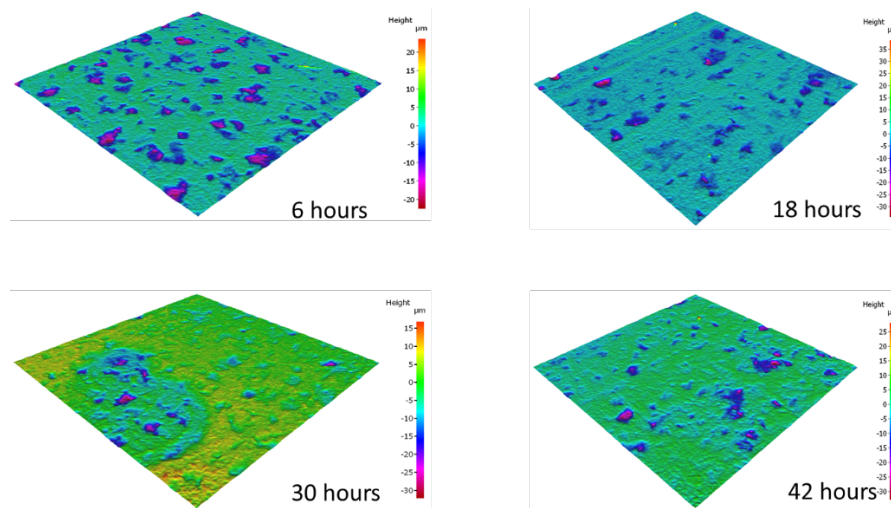


Figure 2. Infinite microscopy characterizations on the metal surface under salt fog exposure.

In the next quarter, UAkron will continue working on the corrosion exposure testing, electrochemical measurements, and surface characterizations once the campus is open. UAkron will also start on COMSOL simulation that includes COMSOL model setup and simulation parameters identification.

(e) Task 2. NDE framework development and validation for interactive defect detection and state characterization in both lab and field environments

1. Background and Objectives in the 2nd Quarter

1.1 Background

Interactive defects detection and characterization in metallic pipes is one of the major challenges identified for pipeline integrity assessment. The group here previously has developed/is developing novel NDE and data processing methods for pipeline applications, including internal corrosion inspection using optical structured light 3D reconstruction and rendering techniques that significantly improves the damage detectability, and stress corrosion cracking (SCC) detection using multi-frequency electromagnetic techniques, remote field eddy current (RFEC) techniques, etc. assisted by machine learning (ML). While there are tremendous successes in these techniques, which work well for exposed pipes or “in-the-ditch NDE”, only Shear Horizontal (SH) guided wave testing has been proven to work in NDE of buried pipelines that poses a big challenge in field-testing to understand realistic interacting threats environment. In this task, the MSU NDE team will develop a multi-modal electromagnetic and ultrasonic framework including electromagnetic acoustic transducer (EMAT) for generation of SH waves (low frequency-50kHz to 500 kHz), localized Rayleigh wave measurement using EMATs and air coupled transducers, and contact ultrasonic measurement for validation of guided wave results for better characterizing the identified interactive anomalies, as well as leveraging other techniques being developed by the group through the other successful programs sponsored by PHMSA. Defect localization and material characterization have always been a challenge for guided waves inspection in this community; and it is worth noting since SH waves have very little out-of-plane leakage, their energy is confined within the pipe walls and they can propagate for long distances. Therefore, any local changes to thickness or material degradation (loss in stiffness and density) can be detected using SH waves, which makes it a perfect candidate for the proposed corrosion/SCC/fatigue defects interaction study. Expanding from the ongoing PHMSA project, introduction of SH waves modality and dedicated signal processing algorithms for analyzing the interactive-damage-feature-encoded data will be crucial for the success of the proposed work.

1.2 Objectives in the 1st Quarter

Across the past quarter, we looked at the effect of corrosion as axial defects (i.e., defects along the length of the pipes). But very often, pipelines are seen to have circumferential defects. In this quarter, we have investigated such defects along the circumference of the pipe. A similar study in terms of characterizing pit depths and number of pits is carried out with the help of circumferential guided waves. The other part of the work involved designing an automated signal classification algorithm that can detect NDE responses from healthy and faulty Pipelines. The final objective for this algorithm is to not only detect an NDE response accurately, but also predict defect characteristics like pit depth, length and location in the pipe.

2. Research Progress in the 2nd Quarter

2.1 Recap of the 1st Quarter Research

In the past quarter, we primarily looked at present techniques for simulating guided waves in pipelines that include the plate wave equation to determine dispersion of guided waves. Meanwhile, modeling defect accurately was also considered crucial in the simulation studies, since the NDE responses based on the modeled defects will be used to optimize the sensor frequency. We used finite element modeling (FEM) to accurately model and mesh defect geometry to study the resulting ultrasonic NDE response. Using FEM helped in not only optimizing sensor parameters (e.g., frequency), but also in studying the physics behind the interaction of guided waves with complex interacting defects, and the generation and reception of guided waves in pipelines.

Structural health monitoring (SHM) of pipelines using ultrasonic required a good understanding of defect signal vs. no-defect signal. While experiments can be carried out to understand this response, one should use a large set of data to effectively understand the differences. It would be rather efficient to rather develop an array of numerical models, which can simulate different materials and structural conditions to obtain

their corresponding ultrasonic response for the complex anomaly scenario. This can further be used to develop the NDE and SHM protocols. In the last quarter, we showed the successful propagation of Ultrasonic Guided Waves (UGW) in a pipeline using a 2-D FEM based model, and also modelled corrosion pits and look at its respective ultrasonic NDE response. The idea behind this was to come up with a model and find the optimum parameters like frequency, excitation etc., that can be then utilized directly in models with realistic defect profiles that is to be developed/generated by the research group at UAkron. It also gave us a clear idea between a defect and a no defect response that was desired before further extensive studies could be studied. We were also able to study the effect of pit depths, and number of pits. Some the results are shown and discussed below for a quick recap.

We modelled a 2D asymmetrical model in COMSOL ® 5 Multiphysics software, where we modelled corrosion as hemispherical pits or cavities of certain depths and lengths. Figure 3 shows the burst excitation that is applied on the transducer boundary in our 2D asymmetrical model. The response for such corroded samples and clean samples were captured, and their simple difference gave rise to the pure defect signature arising from purely the corrosion pits. Also, since these pits/cracks normally exist in interactive colonies, the effect of number of pits has been studied. The material used was the normal Steel AISI 4340 usually found in many pipelines.

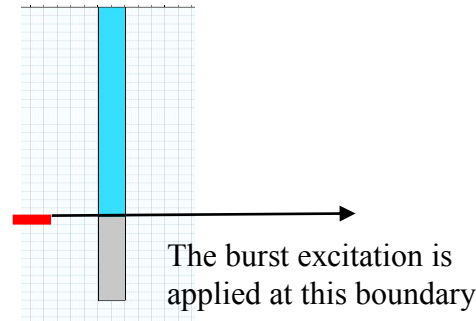


Figure 3: Zoomed simulation model showing the excitation by the application of the burst type signal on transducer boundary.

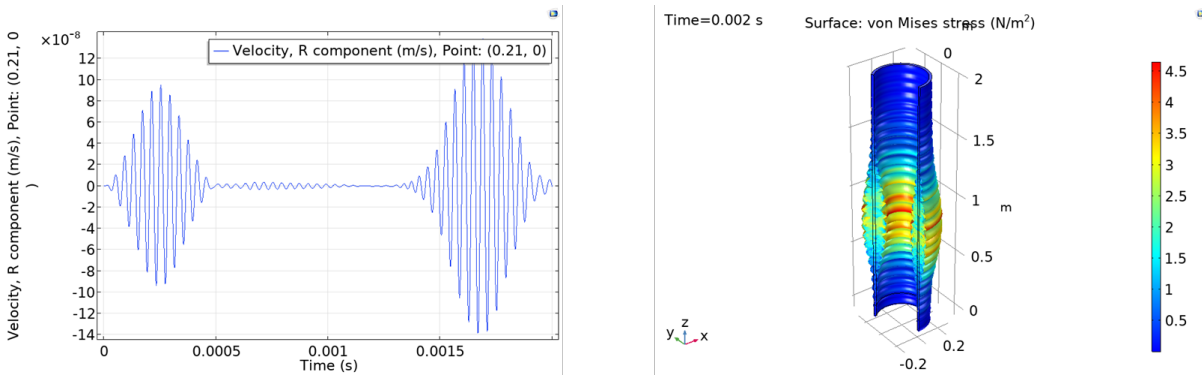


Figure 4: (a) A-scan at (0,0) and (b) von misses stress at time $t = 0.002s$

Figure 4 shows the velocity response of a pipe with an axial defect of 10mm in length and 1 mm in depth, while the Figure 4(b) shows the propagation of Von Mises stress inside the 3D pipe. Figure 5 below gives the comparison of NDE responses between a healthy signal and a defect signal. Clear difference in signals was observed for the pipe with a defect. Taking the difference between these two signals in Figure 5 gives the defect signature arising directly from the defect. We have neglected the mesh noise to simplify the analysis. Figure 6 shows the defect signature.

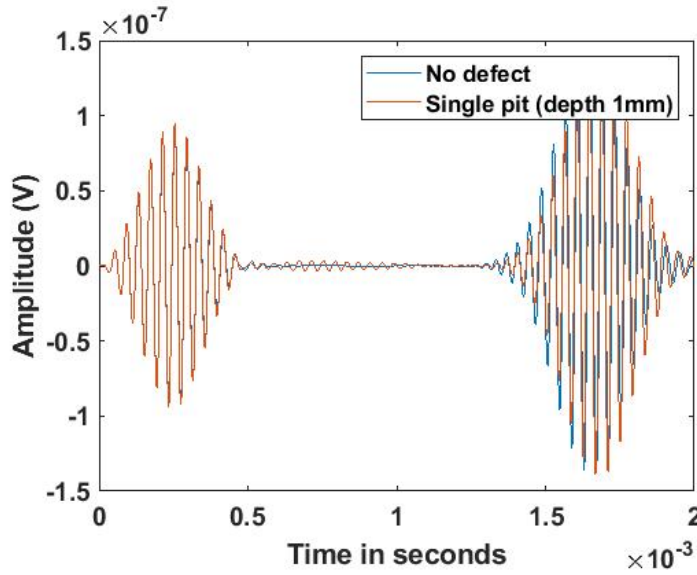


Figure 5: Comparison of A-scans with baseline

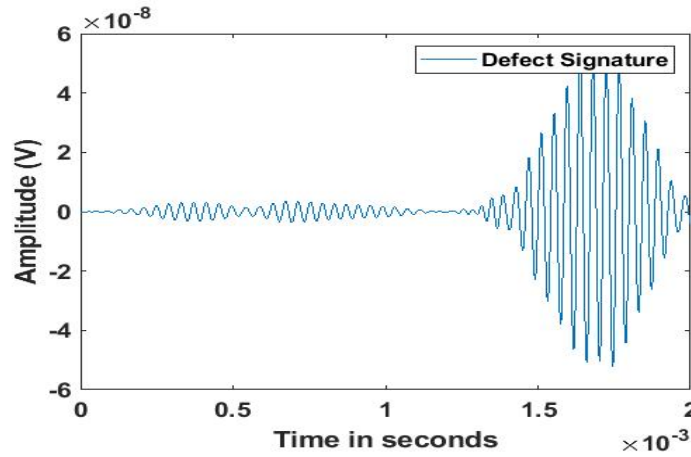


Figure 6: Defect Signature for pit with 1 mm depth

The mechanics of corrosion and how it affects surfaces is a complex process. Hence, predicting the growth of pits requires an extensive field and experimental study. The relationship for pit depth and time for a metal is loosely given as [1],

$$d_{pit} = kT^{1/3}$$

where d_{pit} is the pit depth, T the exposure time and k some constant based on the water and alloy composition. Figure 7 below shows the effect of pit depth on the defect signature. A clear increase in the amplitude of the defect signature was seen. This was expected, because as the pit depth increases, the reflections from the pits are much stronger, and since we used a pulse echo setup, the reflections are much stronger. A similar argument can be made if the number of pits increase, and this is clearly reflected in the defect signatures seen in Figure 8.

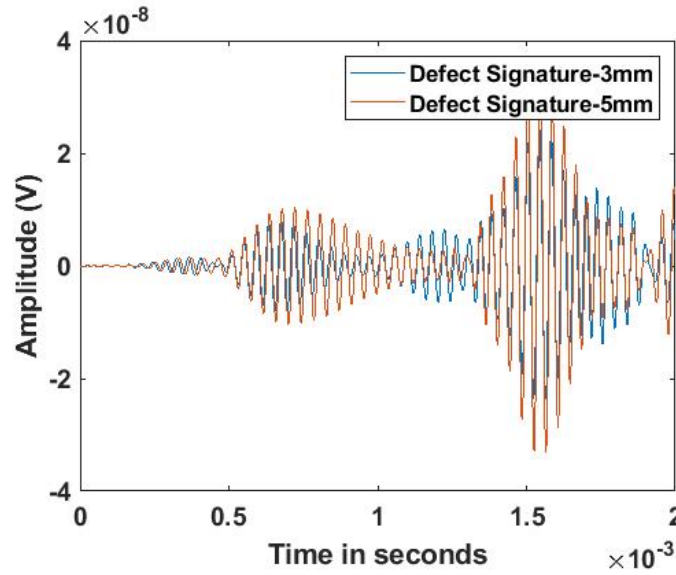


Figure 7: Defect signatures for pits with 3mm and 5 mm depths

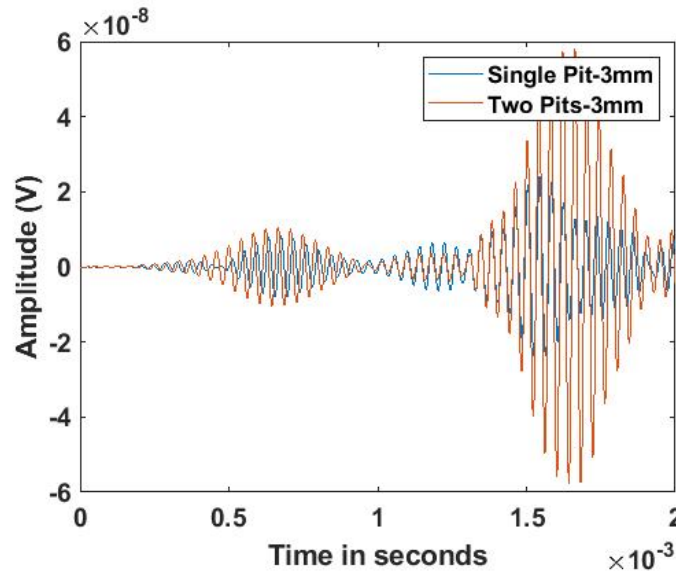


Figure 8: Defect signatures for single and double pit models.

2.2 Circumferential Guided Waves

Circumferential guided waves have an advantage of limited area to be covered depending on the circumference. Thereby, dispersiveness of the waves do not hold any limitation for the interrogation giving the operator freedom to choose any frequency. Circumferential guided waves are lamb waves that are launched using specific arrangement of transducers like the axially arranged phased array elements [2]. Such waves are different than the one-dimensional waves in tubes [3]. Commercial hand held scanners [4] are available that utilize such linear array to scan the pipe length with its axial movement. We consider such a transducer as a point source in the study to study the circumferential guided wave interaction with corrosion. Consider a case of wave propagation along the circumferential direction at a frequency of 50 kHz in a 6 mm thick steel pipe with a diameter of 200 mm. The geometry and defect types are shown in Figure 9. The location of a piezoelectric wafer type transducer at 0° along the circumference and defect location is shown in Figure 9(a). Figure 9(b) shows the pit formed by the Boolean subtraction of three circles from the surface of the pipe. Figure 9(c) shows three pits with a central spacing of 6 mm. Figure

9(d) shows a simulated interactive defect formed by combination of corrosion pit and a crack. Colony of 3 pits with the location of crack in the central pit has been considered. The length of the crack is 2 mm deep. Detection of single and two pit colony has also been considered which has not been shown in the figure. The crack length in Figure 9(d) is changed to 1 and 3 mm to simulate the effect of crack depth on guided wave propagation.

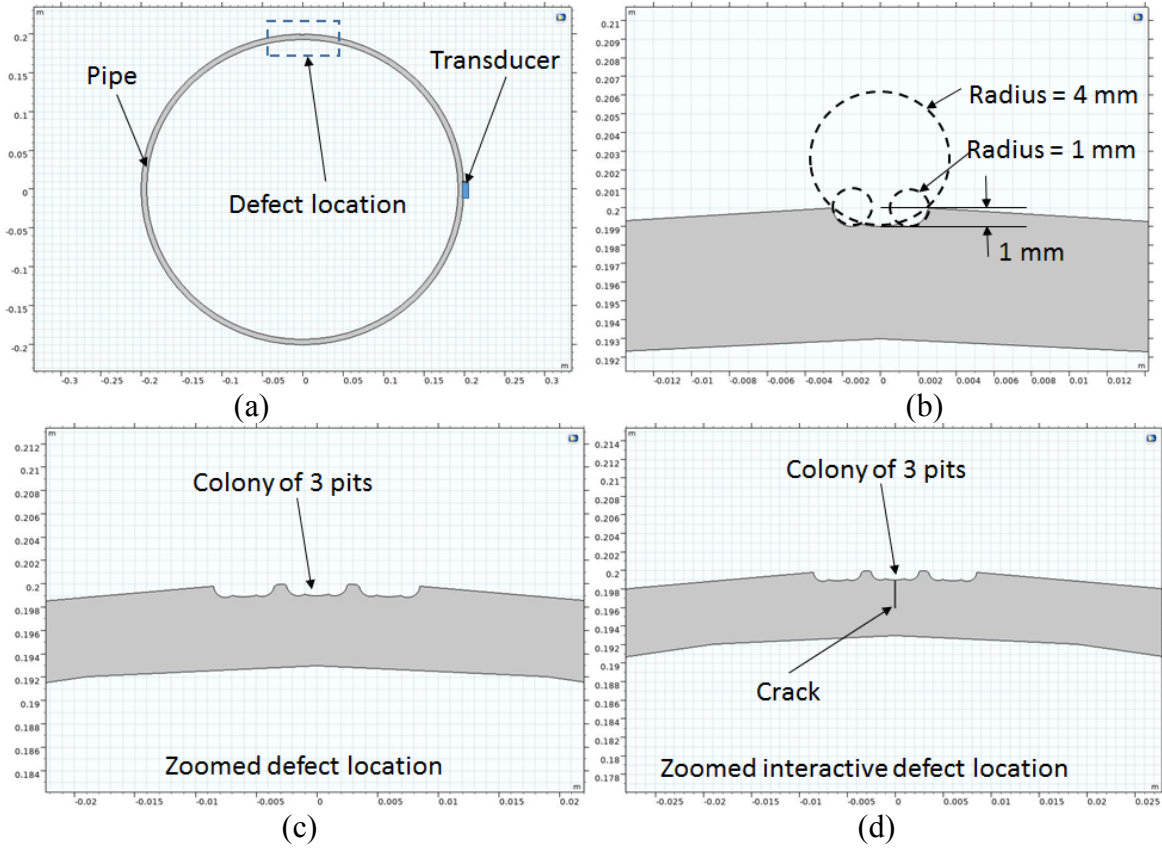


Figure 9: Corrosion type defects located circumferentially around the pipe. (a) Zoomed image showing dimensions of a single pit (c) colony of three pits and (d) interacting defects consisting a colony of three pits with 2 mm deep crack in the central pit.

Results and Discussion

Excitation applied across the wafer type transducer produces S0 and A0 guided waves in the pipe that propagate around the circumference as shown in Figure 10. The pipe being defect free has a wave propagating in both directions from the wafer exciter. With a higher velocity the S0 wave propagates towards another end leaving behind the slower moving A0 wave mode. The top and bottom section of the pipe has similar wave propagation pattern due to symmetric geometry and transducer arrangement. The von Mises distribution is captured at 0.14 ms, which is enough to see the separation of the S0 and A0 wave modes. The wave modes would travel all the way around the circumference and reach the exciter when there are no defects or other structural features obstructing them. The signal received by the same wafer exciter in case of a healthy pipe is shown in Figure 11. The first packet is the incident packet appearing when the wave is launched by the exciter itself. Following packets are the S0 and A0 wave modes respectively returning to the exciter after propagating through the circumference. The signals obtained in the presence of corrosion pits have been superimposed. Clearly the signals vary due to the reflections of S0 wave mode from the corrosion. The reflected packet from the A0 wave mode is mixed with the returned S0 and A0 wave response and requires further processing to obtain it. The single pit produces enough change in the signal to be detected in the presence of a real environment with ambient noise. The reflected wave packet amplitude changes with its spread as the pits increase. This serves as a good indicator of damage severity which can be estimated by a cumulative damage index [5].

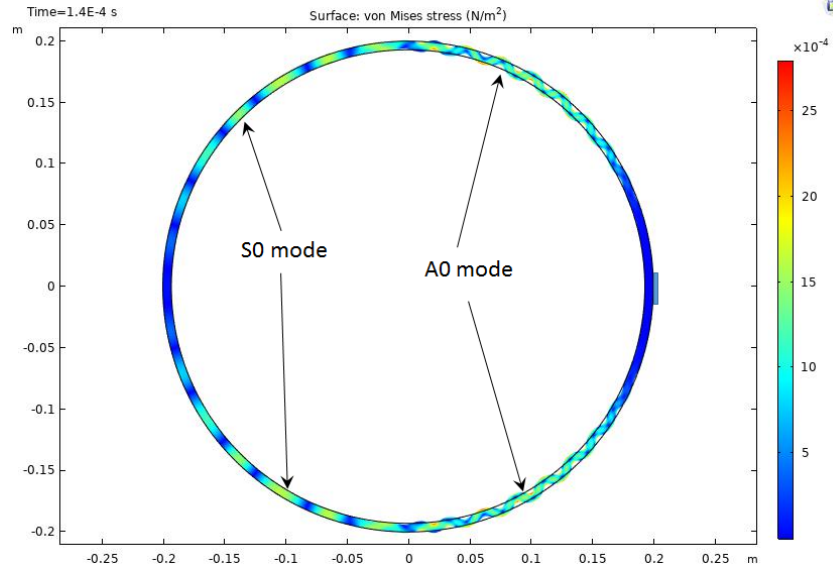


Figure 10: Circumferential guided wave around the pipe seen from the von Mises stress profile across the cross section.

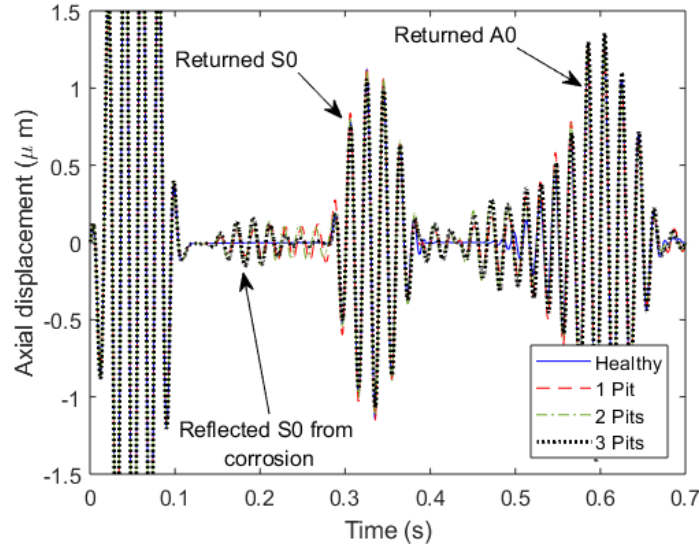


Figure 11: Axial displacement response at the piezoelectric wafer transducer location with healthy, one pit, two pit colony and three pit colony conditions.

Assuming that the three-pit colony is enough to introduce stress corrosion cracking, a crack is introduced at the middle pit with depth of 1 mm. The crack depth is further increased in steps of 1 mm to obtain another two cases of severity. Such interactive damage produces signals shown in Figure 12. The reflected S0 wave mode packet significantly increases in amplitude. The reason is attributed to the reduced cross section causing proportionate reflection of S0 wave energy. The change in amplitude and waveform with frequency content can be further studied for damage classification including interactive features. This aspect is proposed to be done in the next quarter.

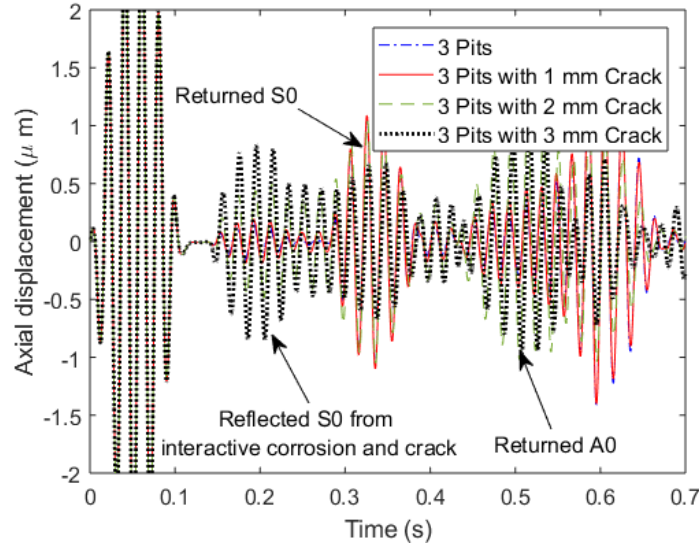


Figure 12: Axial displacement response at the piezoelectric wafer transducer location with three pit colony, interactive 3 pit colony with 1 mm crack, interactive 3 pit colony with 2 mm crack and interactive 3 pit colony with 3 mm crack conditions.

2.3 Automated Signal Classification

Simultaneously, the next step was to automate this process of feature selection, and have a classification algorithm that can effectively predict the defect characteristics given a waveform. The advent of Machine Learning in signal processing, and especially in Nondestructive Evaluation has greatly helped this purpose. Neural Networks in brief are known as universal function approximators [6]. But, for a complicated mapping, an exponential number of hidden units are required but such a large neural network may fail to train. Telgarsky [7] has investigated the importance of depth in neural networks. Deep neural networks encode a general belief that every function can be represented in terms of simpler functions and their combination can approximate the existing function. The underlying features can be extracted from the signal which has reduced a hectic and a time-taking feature engineering process [8]. Each deep learning algorithm has its own pros and cons for wave response as features and is investigated by Rautela and Gopalakrishnan [11]. Hence, choosing the right framework, architecture and the hyper parameters is a challenging task in itself. Deep learning techniques work by feed-forward propagation of input information to hidden layers to get some output. This output is not necessarily a true output (in a supervised learning setting). A back-propagation algorithm flows information backward (which is generally a loss value described by a cost function) while using a gradient descent-based optimization algorithm. During the procedure of continuous forward and backward passes, the learning parameters (weights, W and biases, b) are tuned to a value that minimizes the cost function [9].

Current literature is bent towards abovementioned optimization schemes but here, we have focused on using the Adam optimization. Adam is an adaptive learning rate optimization algorithm that's been designed specifically to train deep neural networks. Adam is a combination of RMSprop and Stochastic Gradient Descent (SGD) with momentum. It utilizes the squared gradients to adaptively scale the learning rate like RMSprop as well as the moving average of the gradient (instead of the gradient itself) like SGD with momentum [10]. A neural network-based learning algorithm maps feature space to target space by minimizing the loss function using a optimization scheme (Adam optimizer here) over a virtual surface created by the dataset in n -dimensional vector space. A typical loss function is the mean-squared loss function (MSE). The formulation is presented in equation below.

$$J(W, h) = \frac{1}{m} \sum_{m=1}^m L(y, \hat{y})$$

A very important aspect while building such automated classification schemes is to collect a good ‘distinguishable’ dataset. By ‘distinguishable’, the dataset should contain signals that have features which vary for different conditions. Any neural network at the end of the day, is a function approximator, and if there is no function to approximate i.e. when similar data is present, the networks fail. An important precursor to build accurate classification algorithms is to check the data for different features, and clean it if necessary. The features can range from simple features like temporal energy, peak amplitude, and time of flights to relatively more complicated features derived from Wavelet Transforms, Fourier Transforms and more.

Dataset Analysis

For this work, we have used only models used in the last quarter, i.e. the axial defects models. We collected about 150 samples, which each collected individually were using the COMSOL models from the past quarter. The split up of the 150 samples is as shown below in Figure 13. Data collecting was a time consuming process as each simulation took about 10 minutes, and 150 simulations adds up to about 25 hours of simulations. Hence our dataset is limited when it comes to the actual size. The simulation parameters are the same as reported in the Quarter 1 report. The faulty signals were collected for range of pit depths and lengths. Also, responses with different number of pits were collected.

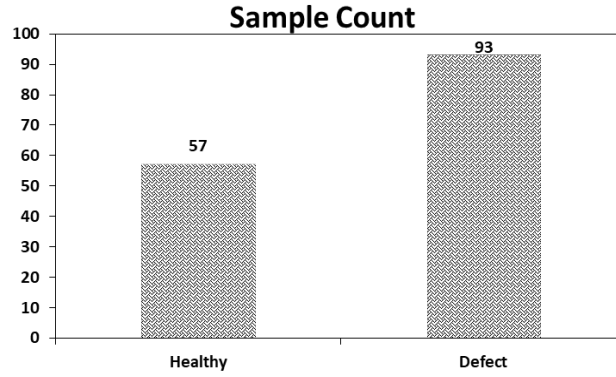


Figure 13: Split of the 150 samples collected for Classification

At first, we look at the simple statistical nature of the data. Simple features like the mean and variance of a vector is computed for all the 150 samples. Figure 14 shows the same. It is clearly seen that there is clear difference in statistics of the NDE responses of the healthy and defect signals.

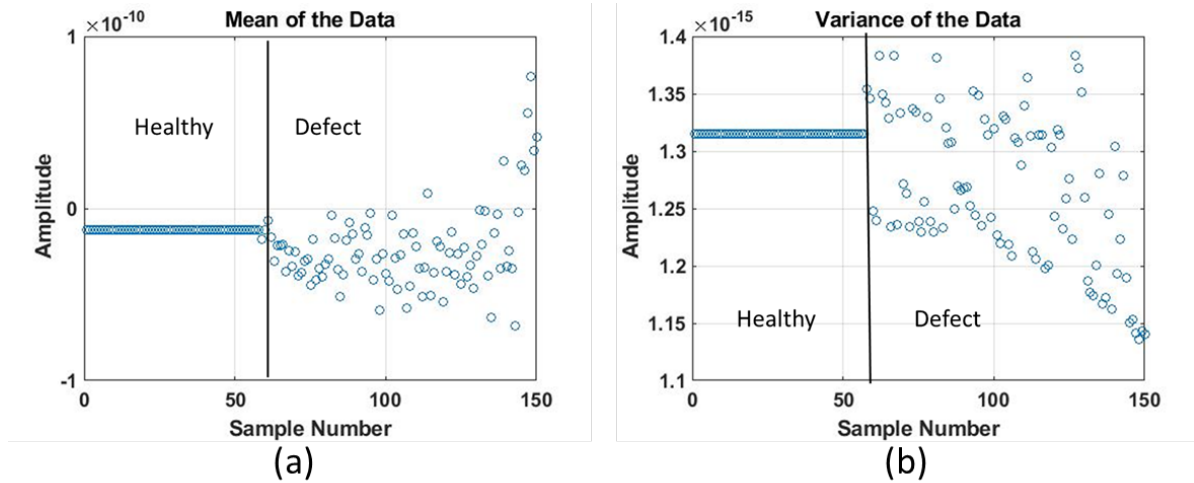


Figure 14: (a) Mean of each sample for the classification dataset and (b) variance of each sample in the dataset (150 samples)

Any NDE response is a time dependent data and also multiple frequencies at different times. Hence it is always important to analyze the temporal and spectral characteristics of such datasets. A simple way would be to look at the spectral and temporal energies of each signal. The formulation for temporal energy is given below.

$$E = \frac{1}{2} \sum_{k=1}^n x_k(t)^2$$

While the spectral energy formulation is as given below,

$$E = \frac{1}{2} \sum_{k=1}^n X_k(f)^2$$

where $X_k(f)$ is the Fourier transform of $x_k(t)$ and is defined as,

$$X_k(f) = \sum_{k=1}^n x_k(t) e^{\frac{-j2\pi kn}{N}}$$

Figure 15 shows the temporal and spectral energy spread for each of the sample. Once again, considerable difference is seen for healthy and defect responses. Kindly note that all 57 responses of a healthy sample is expected to and has similar characteristics, both temporally and spectrally.

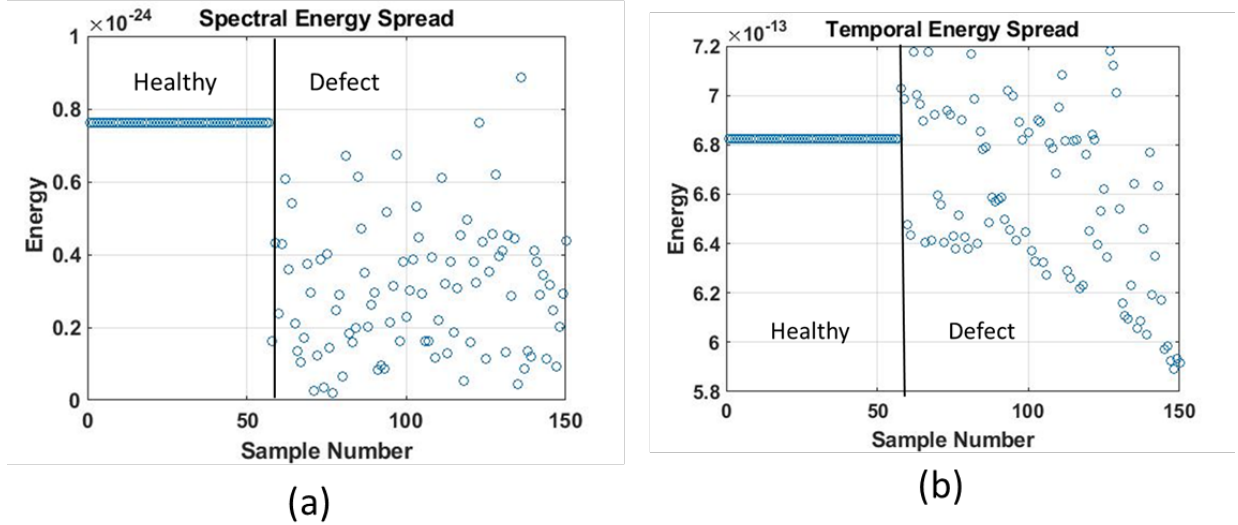


Figure 15: (a) Spectral Energy spread for the classification dataset and (b) Temporal Energy Spread in the dataset (150 samples)

The above analysis has given us a clear picture of the different features that can be potentially used in the classification algorithm. The classification algorithm can be designed in two main ways. One method would be to feed in the raw A-scan itself, while the other would be to feed in the features as separate inputs post processing. The inputs can include the one's discussed above, or go beyond in terms of Wavelet coefficients, Wigner distributions. Feeding in only the features reduces the dimensionality of the problem, and henceforth makes sit computationally more efficient, while at the same time there is a risk if the features chosen don't really most accurately define the characteristics of a healthy or defect sample. This problem is avoided while feeding in the raw A-scan, but it makes it computationally more laborious. In our study, we have fed in the whole A-scan itself as the input, as it is not very clear from the study which

feature influences the outcome most, and without that information, it would be very hard to choose the right set of features to train our network.

Results and Discussion

The first step is to be able to design a network, to simply classify healthy and defect signals in separate classes accurately. We have used a simple Multi-Layer Perceptron Network, whose architecture is described below in Figure 16. The network is trained on 145 samples of the dataset, and is tested 5 randomly chosen samples from the dataset. It consists of 4 dense fully connected layers, with dropout layers to avoid overfitting. By using dropout layers, we ensure the network works well not only to seen data, but also to unseen data. The network predicts a final value to be close to 0 or 1. It is considered a defect if it's close to 1, and healthy if it is close to 0.

Layer (type)	Output Shape	Param #
dense_105 (Dense)	(None, 1039)	1080560
batch_normalization_81 (Batch Normalization)	(None, 1039)	4156
dense_106 (Dense)	(None, 512)	532480
batch_normalization_82 (Batch Normalization)	(None, 512)	2048
dropout_53 (Dropout)	(None, 512)	0
dense_107 (Dense)	(None, 128)	65664
batch_normalization_83 (Batch Normalization)	(None, 128)	512
dropout_54 (Dropout)	(None, 128)	0
dense_108 (Dense)	(None, 1)	129
Total params: 1,685,549		
Trainable params: 1,682,191		
Non-trainable params: 3,358		

Figure 16: Architecture of the Multi-Layer Perceptron Network used.

The loss function used is the MSE function as described previously, while we have used an Adam optimizer. The activation function is Relu. Relu is typically used in neural networks to introduce nonlinearity in terms of the interaction of the inputs which is highly desired in practical problems. It is computed over 100 epochs, with a learning rate of 0.00001. Tuning the hyper parameters is a big aspect of building successful networks, and while there is no such right or wrong techniques to do so, it generally depends on the dataset and the architecture. We evaluate the performance of the network by the Mean Absolute Error (MAE) and the accuracy metric. One of the main takeaways during this was the significance of batch size while training. The batch size greatly influenced the performance of the network. The **batch size** is a hyper-parameter of gradient descent that controls the number of training samples to work through before the model's internal parameters are updated. Since our datasets was small, the chances the networks learn the same type of samples is a possibility. This will lead to over generalization of the problem, and the network won't predict well on unseen samples. Hence with a batch size of four, we were able to achieve very good performance as described below. The training loss curve and the training MAE plot are shown in Figures 17 and 18, respectively.

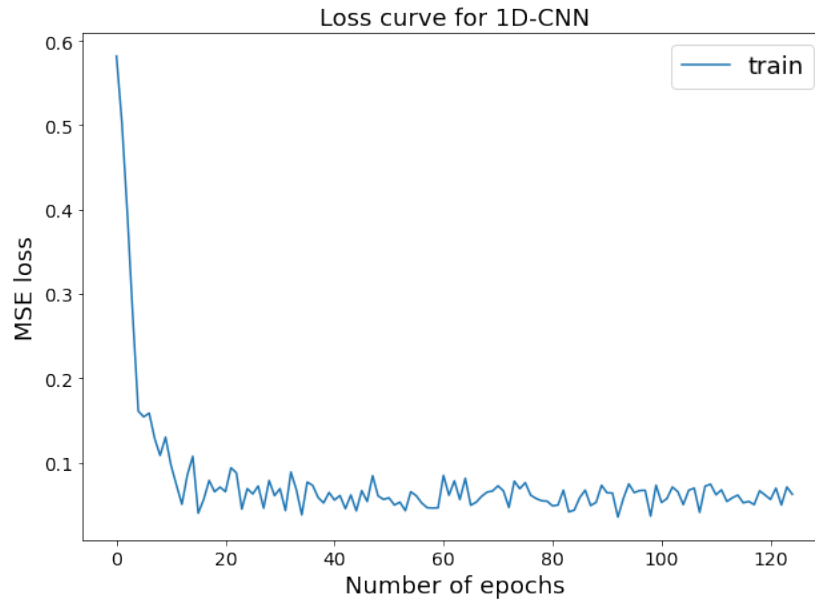


Figure 17: Training Loss for the MLP Network

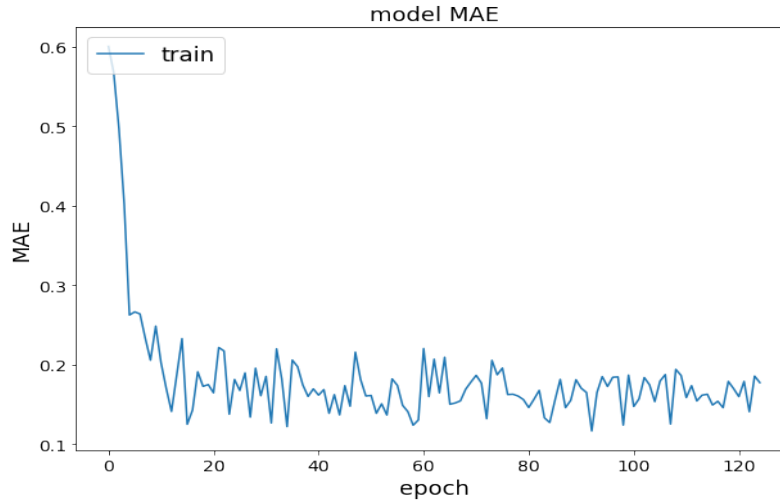


Figure 18: Training MAE for the MLP Network

The loss function converged pretty well during the training, while mean absolute error also converged well. The performance is obviously limited by the fact that our dataset is very small, and it is boosted by the depth of our network. We then used the network to predict the nature of the response on unseen examples, and it predicts with almost 96% accuracy. The accuracy across the training procedure is shown in Figure 19. The jagged nature of the plots in the previous figures (loss, MAE and accuracy) might be probably due to the size of the small dataset. Neural Networks generally need a lot of data to learn and predict very well on seen and unseen examples, and in fields like NDE and SHM, generating or collecting big datasets is a challenge.

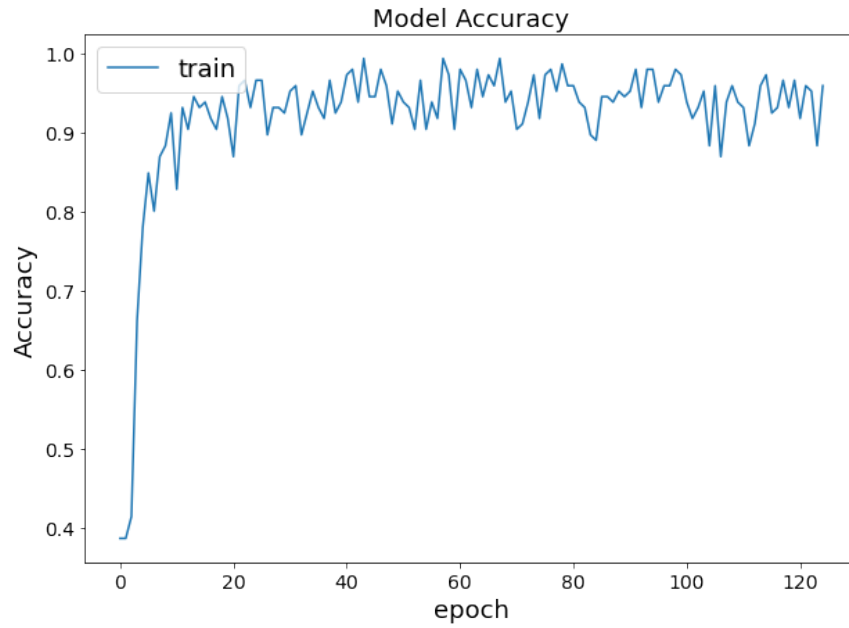


Figure 19: Training Accuracy for the MLP Network

The prediction results for the 5 samples are shown in Figure 20. The network correctly predicts four of the five samples to have defects in them, while it predicts correctly the only healthy sample. Please note that predicting a value close to 0 indicates a healthy sample, while something close to 1 indicates a faulty pipe.

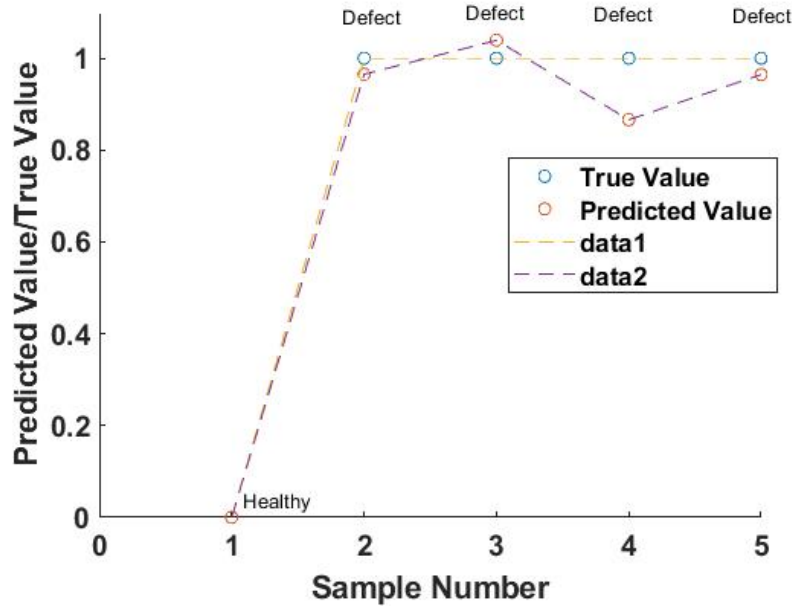


Figure 20: Prediction Results for the MLP Network

2.4 Conclusions

This quarter, we have been able to simulate circumferential ultrasonic guided waves inside a pipe with and without defects in order to optimize the necessary parameters. The interaction of circumferential guided waves in pipes with pits caused due to pitting corrosion has been captured. A comparison of signals with clear defect and a no-defect signal show capability to extract damage feature. The change in defect signatures with respect to pitting depth and number of pits is studied. Also, we were able to come up with an effective classification scheme to classify healthy and defect NDE responses with accuracy. Given any

A-scan, the network can easily predict the health of the pipe. This opens up the prospect of using sensory data (either A-scans or images) to characterize corrosion pits completely. The next question is to develop an algorithm that can predict the characteristics of the defect in terms of its effective area, depth and location. For this, a much larger dataset needs to be collected and more rigorous signal processing schemes in terms of using Wavelet transforms among others

2.5 Future Work

The results obtained by simulating circumferential guided waves hold possibility of determining the damage parameters using a large dataset generated for different pit depths, pit lengths and number of pits, and for different transducer parameters like operation frequency and feature extraction techniques. The simulation results provide results to design a circumferential transducer for experimental validation of these results which will be undertaken in the next quarter. In terms of the furthering a complete classification algorithm, the next step would be developed or improve the existing algorithm to predict defect characteristics like pit depths, length and location. Convolutional Neural Networks seem to work well with time dependent data and regression-based problems. The work is already in progress and almost at completion, and will be presented in the next quarter. The final classification scheme can characterize both axial and circumferential corrosion in terms of the depth, length, area, location and the number of pits. Looking at the bigger picture, other NDE methods like Electromagnetic NDE, Electromagnetic Acoustic Transducers are to be developed to not only characterize corrosion, but any pipeline related defects in general, and have a model that fuses data from different NDE modalities to predict most types of defects in a pipeline and characterize the defect in terms of its most basic characteristics.

(f) Task 3. Probabilistic capacity model development considering interactive anomalies

1. Background and Objectives in the 1st Quarter

1.1 Background

The inaccurate prediction of failure pressure capacity is one of the critical issues in risk management of pipeline systems, as it can impede the ability to achieve a target margin of safety. The burst failure mechanisms for corrosion and cracking defects are fundamentally different, and even more complex for interactive anomalies. With corrosion, the burst failure is a ductile failure due to plastic collapse; with cracking defect, the failure includes ductile failure (similar to corrosion) and brittle failure due to fracture. For a colony of closely spaced defects, the residual strength of a pipeline becomes much lower than an isolated defect due to the interaction among the adjacent defects.

The limitations of existing work regarding the failure pressure predictions include the following: (1) numerous models are available, but no model is universally accepted; (2) the majority of the models were developed based on the concept of a factor of safety, thus, these models are deterministic and cannot be directly used in reliability analysis; and (3) numerous studies have shown that these models provide over-conservative predictions for both corrosion and cracking-like defects, and the bias needs to be quantified and corrected. This Task 3 is aimed to address the limitations mentioned above, and it includes two subtasks:

- Task 3a. Establishment of a failure pressure database
- Task 3b. Probabilistic failure pressure model development

1.2 Objectives in the 2nd Quarter

The overall objective for Task 3a is to establish a database for three groups: isolated and colony of corrosion defects, isolated and colony of crack-like defects, and colony of corrosion and crack-like defects. The overall objective for Task 3b is to develop probabilistic failure pressure models for a pipeline with corrosion anomalies, crack-type anomalies, and interactive anomalies with different types.

In the 1st Quarter, a MS student has worked on establishing a database for isolated corrosion defects (including collecting data from literature and generate new data based on finite element models, FEMs), and reviewing the existing prediction models. In the 2nd Quarter, a Ph.D. student from Dr. Huang's research group, Kiswendsida Jules Kere, was assigned to continue the project to the completion of the project.

The Ph.D. student has checked on the work done by the previous student and found that there are a few things that need to be modified and updated. Therefore, the objectives for Task 3 in the 2nd quarter are to modify the database and fine tune the FEM, and to re-evaluate the performance of the existing prediction models based on the updated database.

2. Research Progress in the 1st Quarter

2.1 Data Collection

The database is for failure pressure of pipelines with isolated corrosion defects, and consists of data collected from literature review and FE analysis conducted in this project. The database collected in the 1st quarter was revised due to repetitive data reported from different literature and other errors found. The total number of burst test results is reduced from 525 to 433. The revised database consists of 83 laboratory experimental burst test results and 350 FEM simulations results.

Furthermore, the additional numerical data were revised based on the modified FEMs, which use ABAQUS Statics-General procedure analysis with Von-Mises criteria as failure criteria. The FEM was then validated using only the experiment test results from the collected database. Table 1 shows the results of the FEM validation.

Table 1. Selected cases for FEM simulation and their results

Reference	Type	Grade	Pipe L (mm)	Pipe D (mm)	Pipe t (mm)	σ_y (MPa)	σ_u (MPa)	d (mm)	l (mm)	w (mm)	P_b (MPa)	FEM (MPa)	Error (%)
[12]	EXP	AISI1020 Mild	420	42	2.73	264	392	1.58	42.00	13.00	37.02	36.66	0.0097
[12]	EXP	AISI1020 Mild	420	42	2.73	264	392	2.24	21.00	13.00	34.55	33.42	0.0328
[13]	EXP	X42	2740	274	4.93	351	454	1.60	45.72	43.02 [†]	14.99	16.24	-0.0833
[13]	EXP	X42	2730	274	4.57	351	454	2.74	66.04	43.11 [†]	12.67	13.03	-0.0286
[13]	EXP	X46	3230	323	8.64	356	469	2.16	63.50	50.79 [†]	24.37	26.71	-0.0959
[13]	EXP	X46	8640	864	9.47	400	508	3.00	185.42	135.65 [†]	10.56	11.18	-0.0589
[13]	EXP	X52	2730	273	5.26	389	502	1.73	139.70	42.89 [†]	18.06	17.76	0.0167
[13]	EXP	X52	6120	612	6.40	433	535	2.57	1371.60	96.05 [†]	9.81	8.20	0.1644
[13]	EXP	X55	5080	508	5.64	462	587	2.46	170.18	79.8 [†]	11.51	11.59	-0.0075
[13]	EXP	X55	5070	507	5.74	462	587	3.02	132.08	79.60 [†]	10.73	11.63	-0.0844
[14]	EXP	X60	3240	324	9.74	452	542	7.14	528	95.3	11.3	10.71	0.0520
[14]	EXP	X60	5080	508	14.8	414	600	9.7	500	95.3	15.8	16.24	-0.0277
[15]	EXP	X65	7620	762	17.5	465	564	8.75	300	50	19.8	20.08	-0.0143
[15]	EXP	X65	7620	762	17.5	465	564	8.75	100	50	24.3	25.85	-0.0638
[16]	EXP	X70	7620	762	15.9	532	627	7.95	300	50	21.5	20.62	0.0408
[17]	EXP	X80	4590	459	8.1	534	661	5.39	39.6	31.9	22.68	22.25	0.0192
[18]	EXP	X80	4590	459	8.00	589	731	3.75	40.00	32	24.20	25.85	-0.0682
[19]	EXP	X100	13210	1321	22.81	782	803	11.31	608.05	207.47 [†]	18.10	18.64	-0.0299
[19]	EXP	X100	13210	1321	22.81	782	803	11.41	1108.13	207.47 [†]	15.40	16.9292	-0.0993

[†] The defect width is assumed to be $0.05\pi D$ based on an assumption from [20]

As shown in Table 1, the selected cases cover a wide range of grade, from AISI1020 Mild (low yield strength) to X100 (high yield strength). The error percentages between the failure pressures reported in the literature and the failure pressures obtained from the FE models are all within 10% except one case where the error is about 16% which is acceptable. The results show that the FE models can be further used to predict failure pressure for other defect scenarios.

2.2 Review of existing prediction models

The grouping of the existing models given in the 1st quarter report was modified, as it is more appropriate to group those models based on the origins of the models. Table 2 provides a summary of the new grouping.

Table 2. Grouping and comparison of existing pressure failure prediction models

Group	Model	Performance comparison within the group
G1: Models based on NG-18	G1-1: ASME B31G Original	G1-7 has the best performance and is suitable for all the levels of the selected quantities.
	G1-2: Modified B31G	
	G1-3: SHELL92	
	G1-4: RPA	
	G1-5: RSTRENG Effective Area	
	G1-6: CSA Z662 2007	
	G1-7: DNV RP-F101	
	G1-8: Fitnet FFS	
	G1-9: Phan et al Modified NG-18	
G2: Models based on Buckingham's π theorem	G2-10: Netto et al. - 2005	G2-11 overestimates the burst pressure and has the worst performance. G2-12 and G2-14 are suitable for Level 2 of the selected quantities.
	G2-11: Mustaffa & van Gelder	
	G2-12: Netto et al. - 2010	
	G2-13: Wang & Zarghamee	
	G2-14: Phan et al Modified - Netto et al	
G3: PCORRC models	G3-15: PCORRC	G3-15 has the best performance.
	G3-16: Modified PCORRC	
G4: RAM PIPE Requal models	G4-17: Original Ram Pipe Requal	G4-17 overestimates the burst pressure and has the worst performance.
	G4-18: Modified Ram Pipe Requal	
G5: Models using strain-hardening	G5-19: Zhu & Leis	Both are suitable for all levels of the selected quantities, but G5-19 perform the best.
	G5-20: Zhu - X65	
G6: Other approaches	G6-21: Choi et al.	All are suitable for Level 2 of the selected quantities, but overall G6-22 perform the best.
	G6-22: Chen et al.	
	G6-23: CUP	
	G6-24: Phan et al. - Modified Gajdoš et al.	

2.3 Results and Discussions

Database analysis

As discussed in the 1st quarterly report, the failure pressure depends on many quantities, such as pipeline material properties and geometry, and defect geometry. Six important quantities: yield strength (σ_y), ratio of pipe thickness to pipe diameter (t/D), ratio of defect depth to pipe thickness (d/t), ratio of defect length squared to the multiplication of pipe diameter and thickness (l^2/Dt), ratio of defect width to defect length (w/l), and ratio of defect width to pipe diameter (w/D), were selected to analyze the database. Due to the revision of the database, the overall range for these six quantities are updated, as shown in Table 3.

Table 3. Data range of six important quantities at different levels

Quantity	Overall Range	Level 1	Level 2	Level 3
		Range	Range	Range
σ_y (MPa)	[262 802]	[262 445]	(445 508]	(508 802]
t/D	[0.0041 0.0652]	[0.0041 0.0157]	(0.0157 0.0207]	(0.0207 0.0652]
d/t	[0.0993 0.875]	[0.0993 0.375]	(0.375 0.550]	(0.550 0.875]
l^2/tD	[0.0183 967.9665]	[0.0183 18]	(18 50]	(50 8967.9665]
$LN(l^2/tD)$	[-4.0002 9.1014]	[-4.0002 2.8904]	(2.8904 3.9120]	(3.9120 9.1014]
w/l	[0.0190 10.9161]	-	-	-
w/D	[0.05 0.48]	-	-	-

The spread of these six quantities over the updated database is shown in Figure 21. Figure 21(a) displays the scatter plot of σ_y over P_b (measured failure pressure) and as expected the result indicates that in general higher yield strength leads to higher burst pressure, except a few cases circled by the dotted lines. It turns out these cases are the ones with high thickness to diameter ratio, t/D , circled by the dotted lines in Figure 21(b) which shows the scatter plot of t/D over P_b . Figure 21(b) also indicates a positive correlation between t/D and P_b .

Figure 21(c) and Figure 21(d) show the scatter plots of d/t over P_b and $\log(l^2/Dt)$ over P_b , respectively. As expected, a negative correlation is observed between the relation d/t and P_b as well as for $\log(l^2/Dt)$ and P_b indicating that the depth and the length of the defect have significant effects on the failure pressure. However, Figures 21(e) and (f) indicate that the impact of defect width may be insignificant on the burst pressure.

Additional Numerical Cases

Using the validated FEM, additional numerical cases are generated and those cases are created to supplement the existing data collected from literature. Figure 22 compares the new FEM cases and the cases collected from literature in terms of the four importance of quantities (σ_y , t/D , d/t , and $\log(l^2/Dt)$). Table 4 summarizes the pipeline property, defect geometries, and obtained failure pressure for those new cases based on the developed FEMs.

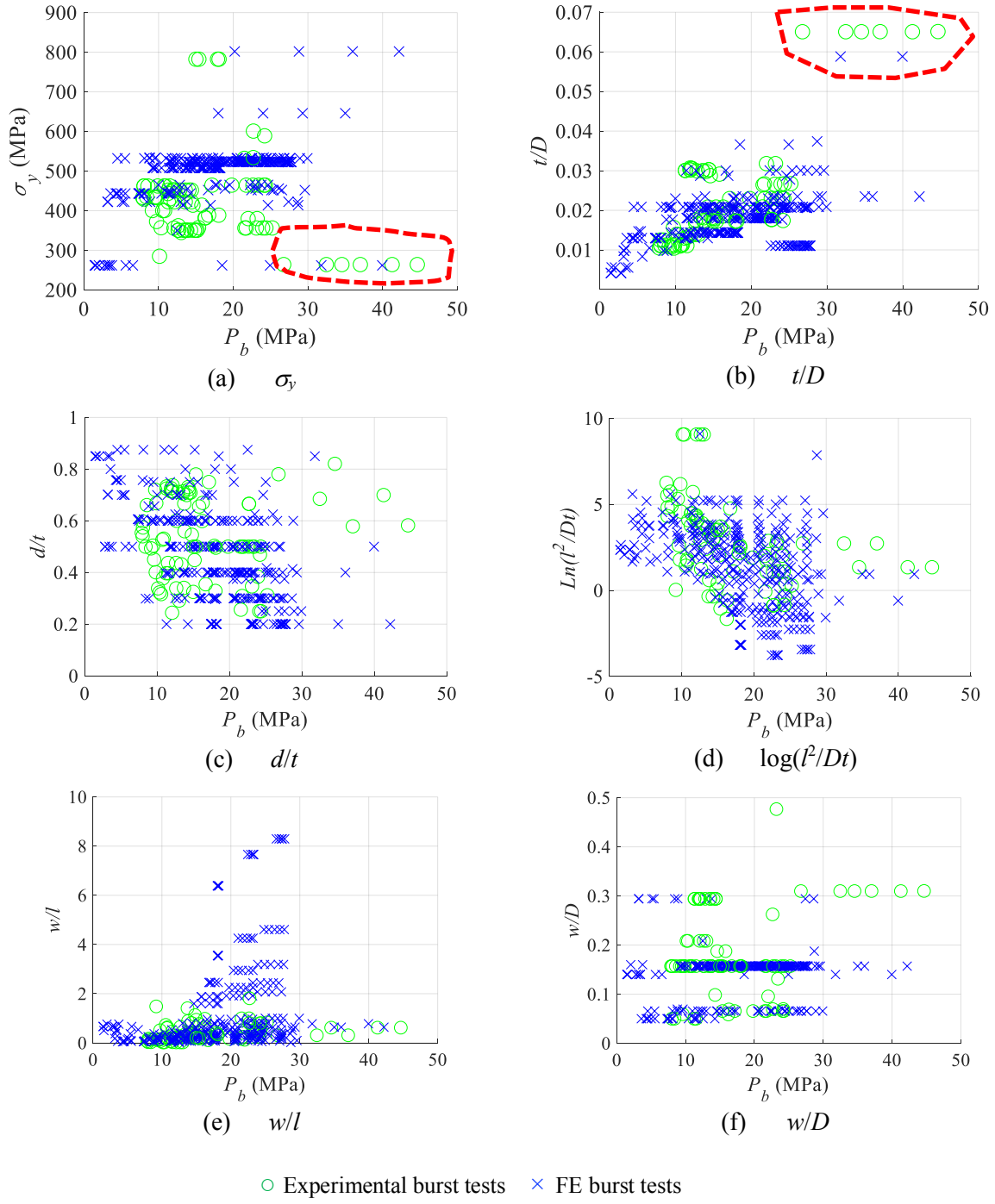
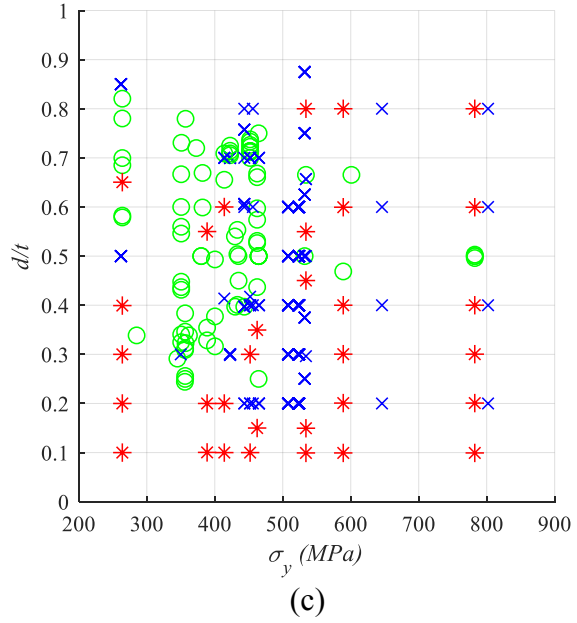
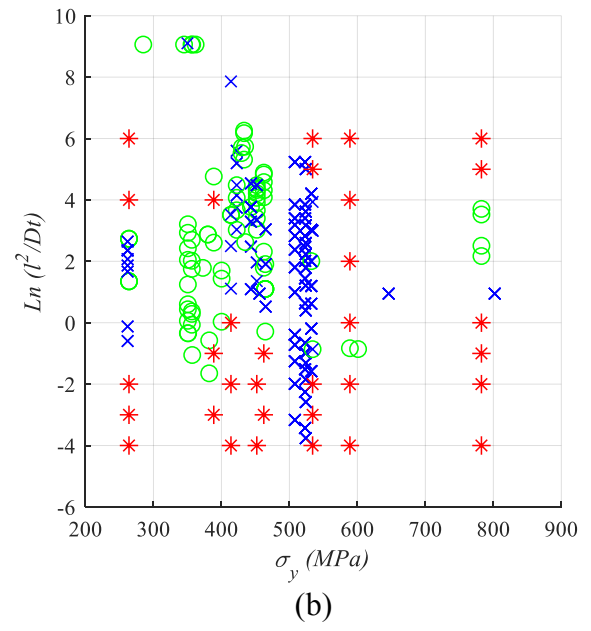
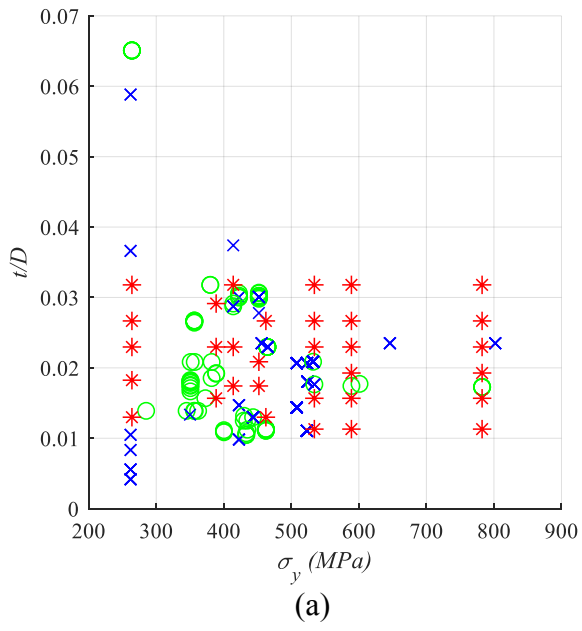


Figure 21: Scatter plots of burst pressure (P_b) vs. selected quantities



- Experimental burst tests from literature
- × FE burst tests from literature
- * New FEM cases

Figure 22: Scatter plots of selected quantities vs. yield stress (σ_y)

Table 4. New cases for FEM simulation

Grade	Diameter D (mm)	Thickness t (mm)	σ_y (MPa)	σ_u (MPa)	d (mm)	l (mm)	w (mm)	Obtained P_b (MPa)
AISI 1020 Mild	508	6.6	264	392	0.66	7.84	79.80	10.60
AISI 1020 Mild	274	5	264	392	1.00	8.26	43.04	14.94
AISI 1020 Mild	762	17.5	264	392	5.25	42.48	119.69	18.64
AISI 1020 Mild	324	8.64	264	392	3.45	390.86	50.89	15.84
AISI 1020 Mild	324	10.3	264	392	6.70	1160.31	50.89	10.67
X52	324	5.08	389	502	0.51	9.05	50.89	17.13
X52	762	17.5	389	502	3.50	70.04	119.69	24.97
X52	508	14.8	389	502	8.14	640.70	79.80	17.42
X60	459	8	414	600	0.80	8.20	72.10	22.88
X60	762	17.5	414	600	3.50	42.48	119.69	29.36
X60	324	10.3	414	600	6.18	57.77	50.89	34.50
X60	459	8	452	542	0.80	8.20	72.10	21.25
X60	762	15.9	452	542	4.77	40.49	119.69	24.23
X55	508	6.6	462	587	0.99	12.92	79.80	16.74
X55	324	8.64	462	587	3.02	32.08	50.89	32.34
X80	508	5.74	534	661	0.57	7.31	79.80	16.43
X80	324	5.08	534	661	0.76	9.05	50.89	22.81
X80	762	17.5	534	661	7.88	42.48	119.69	32.34
X80	324	8.64	534	661	4.75	644.01	50.89	19.19
X80	324	10.3	534	661	8.24	1160.31	50.89	10.19
X80	508	5.74	589	731	0.57	7.31	79.80	18.15
X80	324	5.08	589	731	1.02	14.92	50.89	24.96
X80	273	5.26	589	731	1.58	37.89	42.88	29.09
X80	762	17.5	589	731	7.00	313.90	119.69	28.01
X80	324	8.64	589	731	5.18	390.61	50.89	19.74
X80	324	10.3	589	731	8.24	1160.31	50.89	11.24
X100	508	5.74	782	803	0.57	7.31	79.80	20.51
X100	324	5.08	782	803	1.02	14.92	50.89	28.71
X100	273	5.26	782	803	1.58	22.98	42.88	34.57
X100	762	17.5	782	803	7.00	115.48	119.69	38.22
X100	324	8.64	782	803	5.18	644.01	50.89	20.61
X100	324	10.3	782	803	8.24	1160.31	50.89	12.34

Performance Comparison of Existing Models

Due to the revision of the database, the performance of the existing models is re-evaluated. The performance of a prediction model can be quantified using mean (μ_{res}) and standard deviation (σ_{res}) of residuals (i.e., difference between the prediction and actual values) and mean squared error (MSE). In particular, MSE measures the combination of the bias and variance. Figures 23-26 shows the performance comparisons of the 24 existing prediction models at the three levels of the four quantities (i.e., σ_y , t/D , d/t , and l^2/Dt), respectively, where the crosses refer to μ_{res} , the horizontal lines refer to $\mu_{res} \pm \sigma_{res}$, and solid dots are the MSE values.

As shown in Figures 23-26, regardless the quantities or levels, most model predictions averagely overestimate the burst capacity, resulting in positive μ_{res} , shown as cross markers above the horizontal line of zero residual. Some have negative bias for one level but positive bias for a different level. For example, models *G1-7* and *G5-19* have positive bias for t/D , Levels 1 and 3 (shown in Figures 24(a) and (c)) but negative bias for t/D Level 2 (shown in Figure 24(b)). For the same quantity with different levels, the prediction variance is bigger for σ_y Level-3, t/D Level-1, d/t Level 1, and l^2/Dt Level 1 in general. These results show that the performance of each model changes from level to level. Note that models *G2-11* and *G4-17* overestimate the burst capacity regardless the quantities or levels.

In terms of MSE values, most of models perform better for Level 2 of σ_y (i.e., moderate yield strength), as shown in Figure 23(d). Figure 4(d) shows that most models have worse performance for Level 1 of t/D (i.e., thin pipe thickness). According to Figure 25(d), the models perform similarly in all levels of d/t except models *G2-11*, *G4-17*, and *G4-18*. Figure 26 (d) shows that most of models perform better for Level 2 and Level 3 of $\log(l^2/Dt)$. Table 2 also summarizes the performance comparison of these existing models within their own groups.

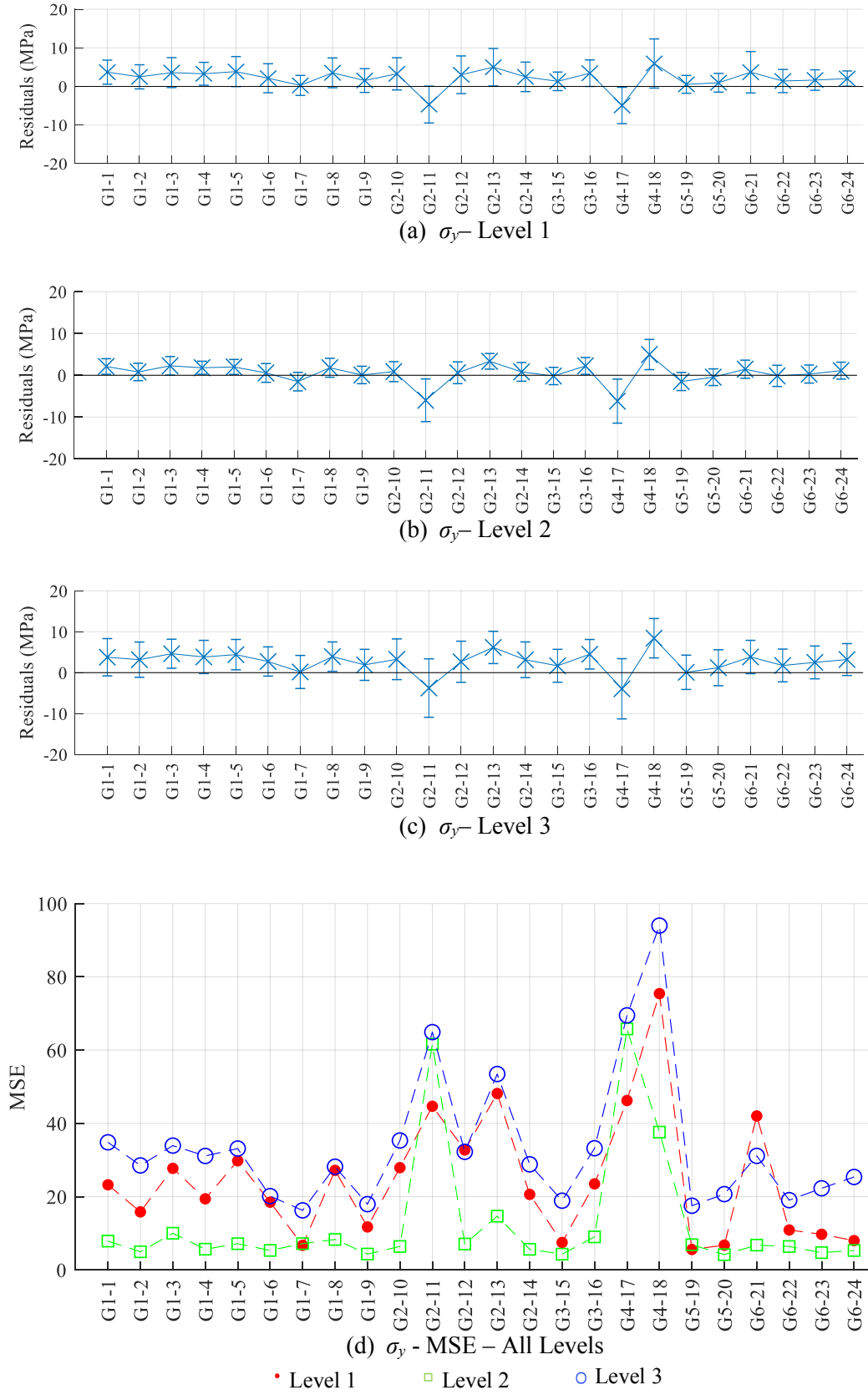


Figure 23: Comparison of residual and MSE of each model for three levels of σ_y

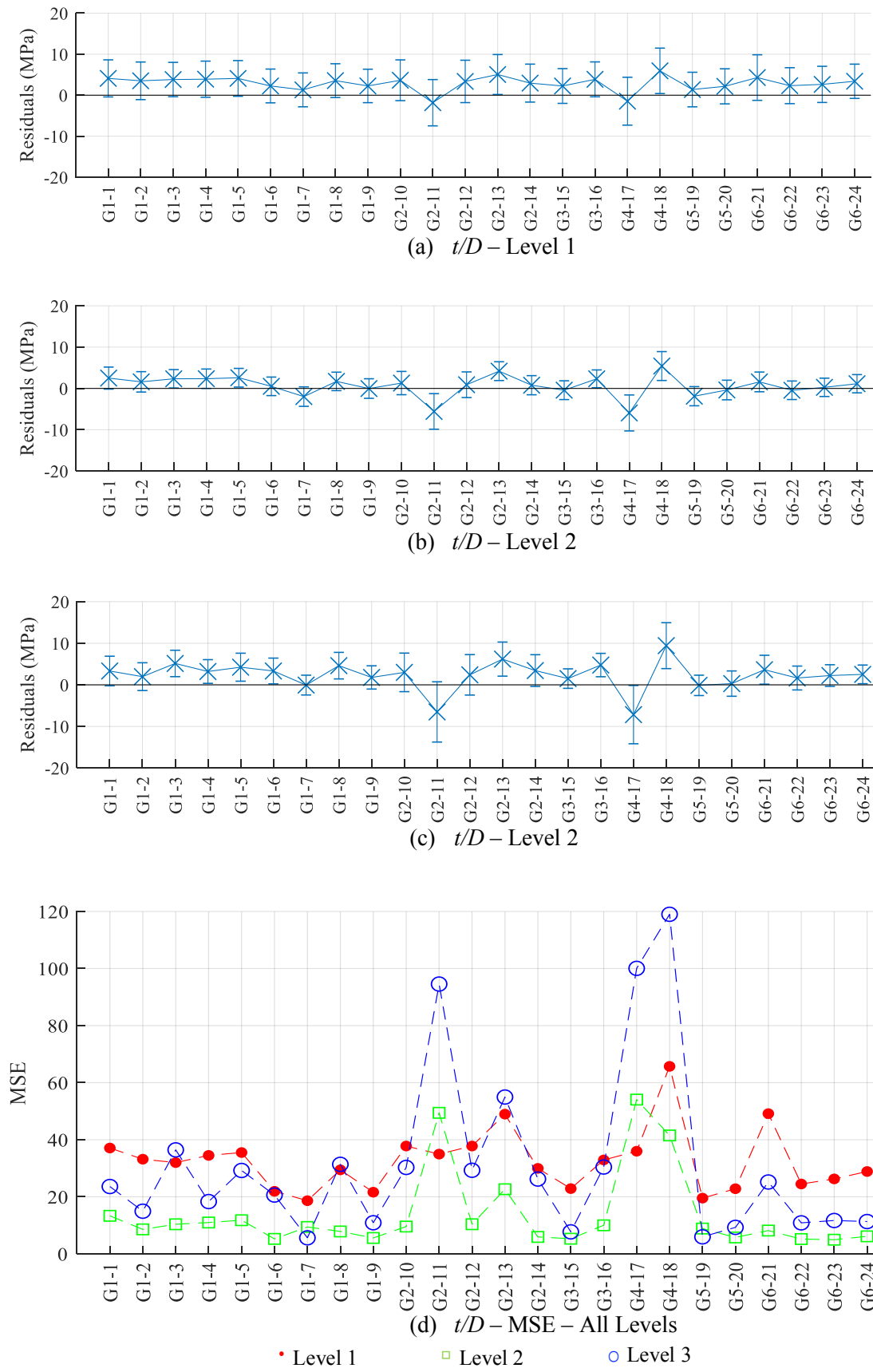


Figure 24: Comparison of residual and MSE of each model for three levels of t/D

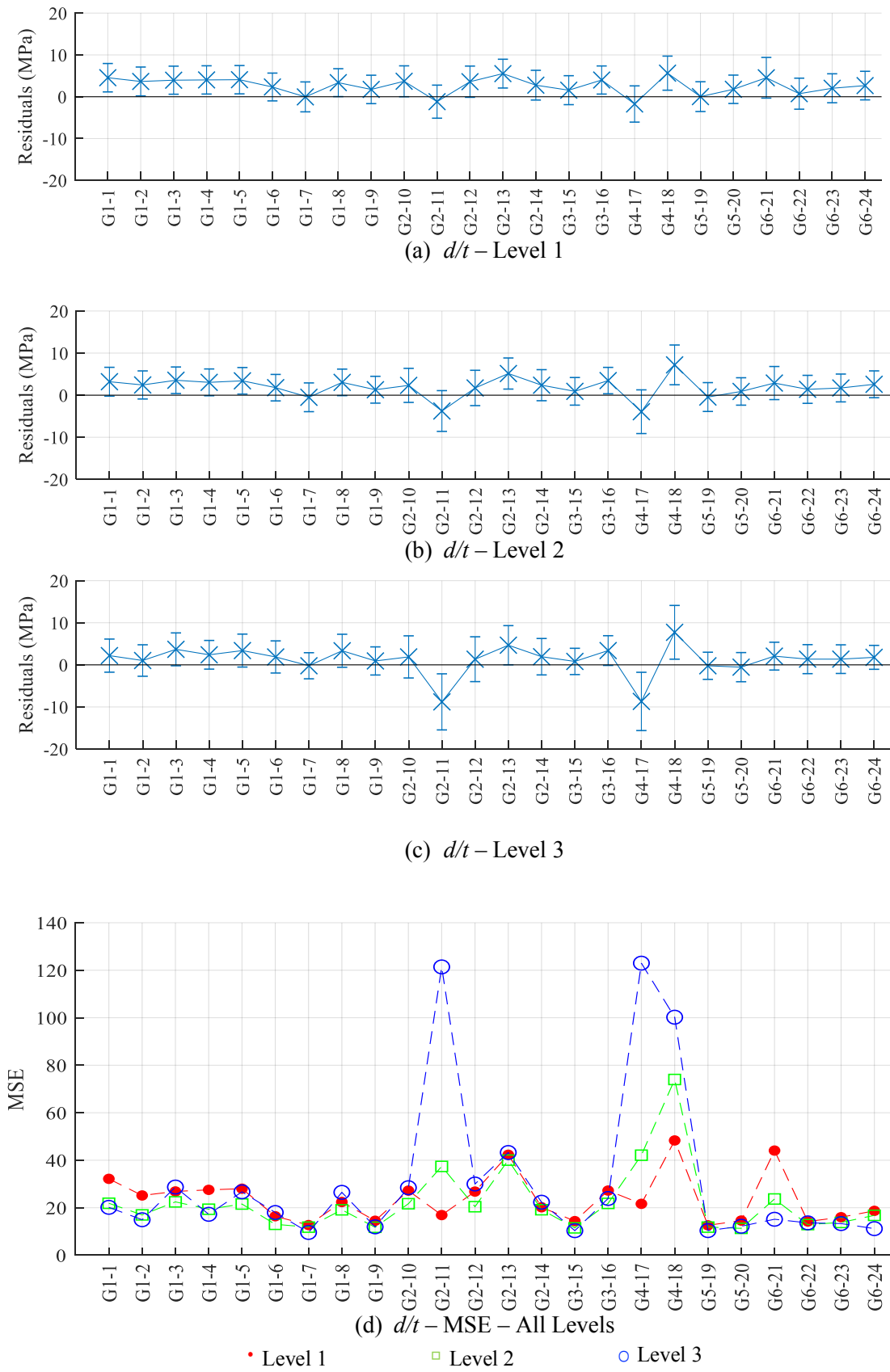


Figure 25: Comparison of residual and MSE of each model for three levels of d/t

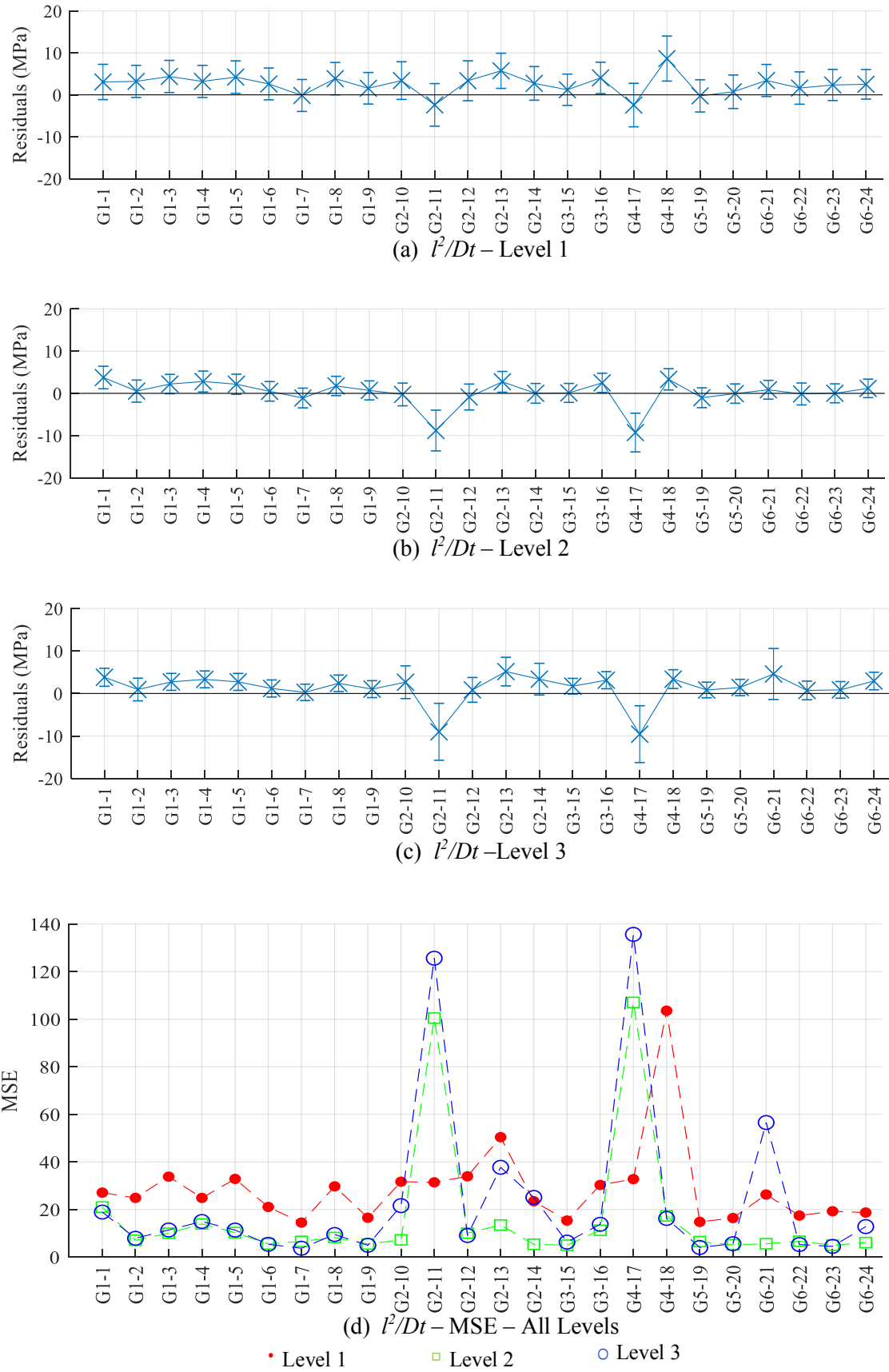


Figure 26: Comparison of residual and MSE of each model for three levels of l^2/Dt

2.4 Future work (next Quarter)

In the next Quarter, the research team will continue working on Task 3. In Task 3a, the colony defect database will be established based on literature review, similar to the database of isolated defect. The FE model will be extended from isolated corrosion defect to colony corrosion defect. In Task 3b, the research team will develop probabilistic burst pressure models for a pipeline with isolated defects based on different levels of yield strength, and possibly to develop the models on different levels of other quantities (such as t/D , d/t , and l^2/Dt). Then the developed models will be compared with the existing models in terms of prediction accuracy using the established database. The impact of the model accuracy on the reliability of pipeline will be also studied.

References

- [1] Godard H. P. (2015). "The Corrosion Behavior of Aluminum in Natural Waters," *Can J. Chem. Eng.*, 39(5), pp. 167–173. [10.1002/cjce.5450380507](https://doi.org/10.1002/cjce.5450380507)
- [2] R. Howard, F. Cegla, Detectability of corrosion damage with circumferential guided waves in reflection and transmission, *NDT E Int.* 91 (2017) 108–119. <https://doi.org/https://doi.org/10.1016/j.ndteint.2017.07.004>.
- [3] J.L. Rose, *Ultrasonic Guided Waves in Solid Media*, Cambridge University Press, 2014. <https://doi.org/10.1017/CBO9781107273610>.
- [4] Innerspec, temate® MRUT, (n.d.). <https://www.innerspec.com/2015/06/06/portable-corrosion-detection-system-qualified-by-oil-majors.html>.
- [5] V.T. Rathod, D. Roy Mahapatra, Ultrasonic Lamb wave based monitoring of corrosion type of damage in plate using a circular array of piezoelectric transducers, *NDT E Int.* 44 (2011) 628–636. <https://doi.org/10.1016/j.ndteint.2011.07.002>.
- [6] Barron AR. Universal approximation bounds for superpositions of a sigmoidal function *IEEE Transactions on Information theory.* 1993 May;39(3):930–45.
- [7] Telgarsky M. Benefits of depth in neural networks arXiv preprint arXiv:1602.04485. 2016 Feb 14.
- [8] Goodfellow I, Bengio Y, Courville A. *Deep learning* MIT press; 2016 Nov 10.
- [9] Rautela M, Bijudas CR. Electromechanical admittance based integrated health monitoring of adhesive bonded beams using surface bonded piezoelectric transducers *International Journal of Adhesion and Adhesives.* 2019 Oct 1;94:84–98.
- [10] Kingma DP, Ba J. Adam: A method for stochastic optimization. arXiv preprint arXiv:1412.6980. 2014 Dec 22.
- [11] Rautela, Mahindra, and S. Gopalakrishnan. Deep Learning frameworks for wave propagation-based damage detection in 1D-waveguides, 11th International Symposium on NDT in Aerospace, Paris. Nov.2019.
- [12] T. A. Netto, U. S. Ferraz, and S. F. Estefen, "The effect of corrosion defects on the burst pressure of pipelines," *J. Constr. Steel Res.* Vol. 61, no 8, pp. 1185–1204, 2005.
- [13] D. Cronin, "Assessment of corrosion defects in pipelines", University of Waterloo, 2000 PhD thesis.
- [14] J. L. C. Diniz, R. D. Vieira, J. T. Castro, A. C. Benjamin, and J.L.F. Freire, "Stress and strain analysis of pipelines with localized metal loss," *Exp. Mech.*, vol. 46, no. 6, pp.765–775, 2000, doi:10.1007/s11340-006-9826-6.
- [15] C. K. Oh, Y. J. Kim, J. H. Baek, Y. P. Kim, and W. S. Kim, "Ductile failure analysis of API X65 pipes with notch-type defects using a local fracture criterion," *Int. J. Press. Vessel. Pip.*, vol. 84, no. 8, pp. 512–525, 2007, doi: 10.1016/j.ijpvp.2007.03.002.
- [16] K. J. Yeom, Y. K. Lee, K. H. Oh, and W. S. Kim, "Integrity assessment of a corroded API X70 pipe with a single defect by burst pressure analysis," *Eng. Fail. Anal.*, vol. 57, pp. 553–561, 2015, doi: 10.1016/j.engfailanal.2015.07.024.
- [17] X. Li, Y. Bai, C. Su, and M. Li, "Effect of interaction between corrosion defects on failure pressure of thin wall steel pipeline," *Int. J. Press. Vessel. Pip.*, vol. 138, pp. 8–18, 2016, doi: 10.1016/j.ijpvp.2016.01.002.
- [18] J. L. F. Freire, R. D. Vieira, J. T. P. Castro, and A. C. Benjamin, "Burst tests of pipeline with extensive longitudinal metal loss," *Exp. Mech.*, vol. 30, no 6, pp.765–775, 2006, doi: 10.1111/j.1747-1567.2006.00109.x.
- [19] V Chauhan and Crossley, "Corrosion assessment guidance for high strength steels (phase1)." [Online]. Available: <https://primis.phmsa.dot.gov/matrix/FilGet.rdm?fil=4877>.
- [20] J. B. Choi, B. K. Goo, J. C. Kim, Y. J. Kim, and W. S. Kim, "Development of limit load solutions for corroded gas pipelines," *Int. J. Press. Vessel. Pip.*, vol. 80, no. 2, pp. 121–128, 2003, doi: 10.1016/S0308-0161(03)00005-X.
- [21] J. F. Kiefner and P. H. Vieth, "New method corrects criterion for evaluating corroded pipe," *Oil Gas J.*, 1990.